The Astrophysical Journal, 837:113 (18pp), 2017 March 10 https://doi.org/10.3847/1538-4357/837/2/113

Dynamics of Coronal Hole Boundaries

A. K. Higginson[1], S. K. Antiochos[2], C. R. DeVore[2], P. F. Wyper[3], and T. H. Zurbuchen[1]
[1] Department of Climate and Space Sciences and Engineering, University of Michigan, Ann Arbor, MI 48109, USA
[2] Heliophysics Science Division, NASA Goddard Space Flight Center, Greenbelt, MD 20771, USA
[3] Universities Space Research Association, NASA Goddard Space Flight Center, 8800 Greenbelt Road, Greenbelt, MD 20771, USA
Received 2016 August 30; revised 2016 December 14; accepted 2016 December 22; published 2017 March 8

Abstract

Remote and in situ observations strongly imply that the slow solar wind consists of plasma from the hot, closed-field corona that is released onto open magnetic field lines. The Separatrix Web theory for the slow wind proposes that photospheric motions at the scale of supergranules are responsible for generating dynamics at coronal-hole boundaries, which result in the closed plasma release. We use three-dimensional magnetohydrodynamic simulations to determine the effect of photospheric flows on the open and closed magnetic flux of a model corona with a dipole magnetic field and an isothermal solar wind. A rotational surface motion is used to approximate photospheric supergranular driving and is applied at the boundary between the coronal hole and helmet streamer. The resulting dynamics consist primarily of prolific and efficient interchange reconnection between open and closed flux. The magnetic flux near the coronal-hole boundary experiences multiple interchange events, with some flux interchanging over 50 times in one day. Additionally, we find that the interchange reconnection occurs all along the coronal-hole boundary and even produces a lasting change in magnetic-field connectivity in regions that were not driven by the applied motions. Our results show that these dynamics should be ubiquitous in the Sun and heliosphere. We discuss the implications of our simulations for understanding the observed properties of the slow solar wind, with particular focus on the global-scale consequences of interchange reconnection.

Key words: magnetic reconnection – magnetohydrodynamics (MHD) – solar wind – Sun: corona – Sun: evolution – Sun: magnetic fields

Supporting material: animations

1. Introduction

Understanding how the plasma and magnetic field of the Sun's atmosphere—from the photosphere to the corona—extend outward to form the heliosphere has long been one of the central goals of heliophysics. In his pioneering work, Parker (1958) gave the simplest model for this Sun-heliosphere connection. Parker proved that for a spherically symmetric atmosphere maintained at a roughly constant temperature by some coronal heating process, the plasma would expand outward to form a steady supersonic solar wind. Remote-sensing observations of the solar corona, however, such as the exquisite eclipse photographs of Druckmüller (2009) and the ultra-high-resolution XUV images from *Hinode* and the *Solar Dynamics Observatory* (e.g., Schrijver et al. 2013), show that the solar corona is very far from spherical symmetry due to the action of the Sun's magnetic field. The field adds structure and dynamics to the basic picture proposed by Parker, affecting both its large-scale organization and the thermal properties of the solar wind through small-scale dynamics.

The most fundamental structure introduced by the field is the existence of magnetically "closed" and "open" regions. In closed regions, the field lines have a finite length and connect at both ends to the photosphere, confining the plasma. In open regions, the field lines do not connect back to the photosphere within the inner corona and instead stretch out indefinitely to form the heliosphere. Note that, for a truly steady state, the solar wind can originate only from the open-field regions.

These two types of coronal regions are readily apparent in X-ray/XUV images of the Sun because of the differences in the properties of their plasma. In closed regions, where the plasma is confined, both the density and the temperature tend to be high, $N \sim 1 \times 10^9\,\mathrm{cm}^{-3}$ and $T \sim 1\,\mathrm{MK}$ (Feldman et al. 1978; Laming et al. 1997; Warren & Brooks 2009), whereas in open regions, $N \sim 2 \times 10^8\,\mathrm{cm}^{-3}$ and $T \sim 0.8\,\mathrm{MK}$ (Doschek et al. 1997; Del Zanna & Bromage 1999; Landi 2008). As a result, the open regions are often observed to be dark in X-ray images and are referred to as "coronal holes" (Zirker 1977).

Due to this temperature difference, the plasmas in open and closed regions have different ionic charge-state compositions, which are readily seen in spectroscopic observations of the corona (Doschek & Feldman 1977; Doschek et al. 1997). In addition, open and closed plasmas are observed to have very different elemental compositions. A key result emphasized by Meyer (1985) in his pioneering studies is that the elemental abundances of coronal and heliospheric plasma are sensitive to the first ionization potential (FIP) of the particular element. Many studies have shown conclusively that in open-field regions the coronal plasma has heavy-element abundances close to those of the photosphere. In closed regions, however, the low FIP elements, such as Fe and Mg, have abundances relative to the photosphere that are 4–6 times larger than the abundances of the high FIP elements, such as N and Ar (Meyer 1985; Feldman & Widing 2003; Laming 2015; von Steiger & Zurbuchen 2016).

This striking abundance variation also shows up in the plasma of the solar wind. It has long been known that the solar wind consists of two distinct types: the so-called fast wind, with speeds $>500\,\mathrm{km\,s}^{-1}$, and the slow wind, with speeds $<500\,\mathrm{km\,s}^{-1}$. The fast wind is generally believed to originate in coronal holes. For example, the *Ulysses* measurements show that during solar minimum the wind at high latitudes emanating from the polar coronal holes is all fast wind (Zurbuchen 2007 and references therein; McComas et al. 2008). Furthermore, this wind exhibits

both elemental abundances and ionic charge states indicative of a source near the Sun that is similar to coronal-hole plasma (Geiss et al. 1995; von Steiger et al. 2000). Latitudinal scans by *Ulysses* have shown that the fast wind exhibits little spatial variation in speed and composition over large coronal holes. Consequently, it can be thought of as the quasi-steady wind predicted by Parker (1958), although with different physical processes as its source.

The slow wind, by contrast, has very different properties, and its source at the Sun is still an issue of intense debate. It appears to be associated with streamers (Raymond et al. 1997), being limited to low latitudes during the minimum of solar cycle 23 (Manoharan 2012), when the streamers were also found only at low latitudes. The slow wind extended further during the more complex solar minimum of cycle 24 (Tokumaru et al. 2010), when streamer structures also extended to higher latitudes. It is also associated with the heliospheric current sheet (HCS) emanating from the top of the closed-field region (Gosling 1997; Zhao et al. 2009). Indeed, the HCS is always embedded in the slow wind, never the fast (Burlaga et al. 2002). The location and composition of the slow wind suggest that it is somehow associated with the closed-field regions. Furthermore, the slow wind has an elemental composition similar to that of the closed-field plasma, and its ionic charge states indicate a source plasma with a temperature similar to that of the closed corona rather than coronal holes (von Steiger et al. 1997, 2001; Zurbuchen et al. 1999, 2002). In fact, several authors argue that plasma composition is a much better discriminator between the two types of wind than the flow speed (e.g., Zhao et al. 2009).

The third major feature of the slow wind that distinguishes it from the fast is its variability. The slow wind exhibits continuous, strong variability in all plasma properties, especially composition and density (Gosling 1997). This variability appears to be related to specific structures and not the consequences of simple Alfvénic turbulence observed in the fast wind. In fact, recent results by Viall & Vourlidas (2015) and Kepko et al. (2016) indicate that 85% or more of the slow wind consists of quasi-periodic structures that vary rapidly, on timescales of hours, in both density and plasma composition. Accompanying these plasma variations is a strong variability in the magnetic field measured at 1 au with clear signatures of plasmoids and disconnected flux (Kepko et al. 2016). These authors conclude, through a detailed analysis of white-light observations combined with in situ measurements, that magnetic reconnection in the streamer stalks that map down to the closed-field region is the fundamental process giving rise to the quasi-periodic structures.

As a result of the observations described above, especially the composition and variability measurements, many models postulate that the slow wind is due to closed-field plasma that is released onto open field lines (Fisk 2003; Antiochos et al. 2011). This release is believed to occur as a result of the magnetic-field dynamics, specifically reconnection between open and closed flux: so-called interchange reconnection (Fisk et al. 1999; Crooker et al. 2002). There are two main types of magnetically driven dynamical models for the origin of the slow wind. In the interchange model proposed by Fisk and coworkers, open flux is postulated to diffuse throughout the closed regions, releasing closed-field plasma via interchange reconnection (Fisk et al. 1998; Fisk 2003; Fisk & Zhao 2009). It should be noted, however, that the fundamental tenet of this model—that open flux can diffuse deep into closed regions—has yet to be demonstrated by rigorous numerical simulations.

A more widely accepted model is the streamer-top model (Suess et al. 1996; Sheeley et al. 1997, 2009; Endeve et al. 2004; Rappazzo et al. 2005) and its extension, the Separatrix Web (S-Web) model, in which the dynamics are localized at the boundary between the open and closed flux (Antiochos et al. 2007, 2011). The basic idea of the S-Web model is that the driving of the coronal magnetic field by continual photospheric motions must broaden any open-closed boundary—which, for a steady state, is a separatrix surface of zero width—into a finite-width dynamic boundary layer. Magnetic flux in this boundary layer constantly opens and closes as a result of interchange reconnection, with closed flux opening and open flux closing. This boundary layer extends out into the heliosphere to form the streamer stalks and embedded HCS.

It should be noted that the dynamical driving of the open-closed boundary has long been proposed to explain a number of observed phenomena. On global scales, the continual opening and closing of coronal-hole boundaries has been invoked (e.g., Wang et al. 1996) as the mechanism that accounts for the apparent rigid rotation of some coronal holes (Timothy et al. 1975; Zirker 1977). On intermediate scales, interchange reconnection at the separatrices that define the tops of pseudostreamers (Wang et al. 2007) is widely believed to be responsible for the bright plasma sheets in the heliosphere (Hundhausen 1972) that define these structures. Finally, on small scales, reconnection at the open-closed boundary separating small closed-field bipoles from the open flux of polar coronal holes is generally accepted to be the mechanism underlying a broad range of activity, including spicules, plumes, and jets (e.g., Pariat et al. 2015).

Therefore, calculating and understanding the dynamics of the open-closed boundary driven by photospheric motions is essential for understanding a host of observed solar activity and is at the heart of the S-Web model for the slow wind. Since the photosphere is undergoing turbulent convection, its flows cover all spatial scales ranging from the solar radius down to the viscous dissipation scale, but for S-Web dynamics we can consider these flows to have three dominant scale regimes. For global motions (such as the differential rotation or meridional flow) that have timescales of many days, much longer than the typical timescale for setting up a steady wind ($\sim$1 day), the open-closed boundary evolution can be considered as quasi-steady. In the other extreme, the small-scale flows of granules and the magnetic carpet (Schrijver et al. 1997), which are of order minutes, are much smaller than a day, so these are likely to produce only Alfvén wave "noise" at the boundary. This noise may play a critical role in heating the plasma and driving the wind, but we do not expect it to be important for releasing the closed-field plasma of the slow wind. The important motions for driving the open-closed boundary are likely to be the supergranular flows, which have timescales of order 1 day or so.

In this paper, we present the first detailed calculations of the dynamical response of a prototypical coronal-hole boundary to driving by supergranule-like motions. To understand the overall topology and physical mechanisms, these first calculations use the simplest structure for the initial coronal magnetic field and the driving motions. As with all numerical experiments, we are limited to a Lundquist number that is orders of magnitude smaller than solar values. This and other numerical issues are addressed in Section 5. However, we have

carefully designed our simulations so that our results can be applied with confidence to the Sun. Although we do not attempt to match exactly the slow speed and small scale of photospheric supergranules, we show that, even with the simplest possible initial open-closed boundary and representation of photospheric driving, the system quickly develops an intricate three-dimensional (3D) structure. This results in complex reconnection dynamics between open and closed flux that should be present at any boundary between a coronal hole and a helmet streamer, lending support to S-Web-type models. We also emphasize that, irrespective of the theoretical model for the slow solar wind, the driving of coronal-hole boundaries by photospheric motions must be a generic feature of the Sun's corona and must be considered when interpreting observations of the corona and wind. As discussed below, the results of this first investigation into these generic dynamics have important implications for understanding how the corona produces the solar wind that we observe.

2. Method

2.1. MHD Model and Initial Conditions

Our calculations use the Adaptively Refined Magnetohydrodynamic Solver (ARMS), which uses flux-corrected transport methods to capture shocks and minimize diffusion (DeVore 1991). Our numerical domain consists of a spherical wedge centered on the Sun, in which we solve the following ideal magnetohydrodynamic (MHD) equations:

$$\frac{\partial \rho}{\partial t} + \boldsymbol{\nabla} \cdot (\rho \boldsymbol{u}) = 0, \tag{1}$$

$$\frac{\partial \rho \boldsymbol{u}}{\partial t} + \boldsymbol{\nabla} \cdot (\rho \boldsymbol{u}\boldsymbol{u}) = \frac{1}{4\pi}(\boldsymbol{\nabla} \times \boldsymbol{B}) \times \boldsymbol{B} - \boldsymbol{\nabla} P + \rho \boldsymbol{g}, \tag{2}$$

$$\frac{\partial \boldsymbol{B}}{\partial t} - \boldsymbol{\nabla} \times (\boldsymbol{u} \times \boldsymbol{B}) = 0, \tag{3}$$

where ρ is the plasma mass density, $\boldsymbol{u}$ is the plasma velocity, $\boldsymbol{B}$ is the magnetic field, P is the plasma pressure, and $\boldsymbol{g} = -GM_{\odot}\boldsymbol{r}/r^3$ is the gravitational acceleration. The plasma pressure is calculated from $P = 2(\rho/m_p)k_{\rm B}T$, i.e., we assume the simplest solar atmosphere of a fully ionized hydrogen gas at a constant, uniform temperature, $T = 1$ MK. ARMS stores the variables on a staggered grid to keep the divergence of the magnetic field fixed at zero to machine precision. It solves the equations using a second-order predictor/corrector in time and a fourth-order integrator in space. Together with the flux limiter, this ensures that magnetic reconnection via numerical diffusion takes place only in regions where the magnetic field develops structure down to the scale of the grid. In these locations, the effective numerical resistivity is determined by the flow speed and grid spacing. Since the main numerical challenge for our simulations is to resolve as much structure as possible with limited computational resources, we do not include an explicit resistivity.

The initial magnetic field is calculated using the Potential Field Source Surface (PFSS) model (Altschuler & Newkirk 1969) for a dipole at Sun center. The dipole strength is chosen so that the magnetic field at 1 $R_{\odot}$ is equal to 10 G at the poles, which is a good estimate for the quiet-Sun magnetic field (Long et al. 2013). The radius of the source surface, beyond which the initial magnetic field is assumed to be radial, is set at $R_S = 3R_{\odot}$ (Schatten et al. 1969). As discussed below, this initial field is then allowed to equilibrate with the initial atmosphere and solar wind to reach a new quasi-steady equilibrium before the system experiences any driving.

For the initial atmosphere, we use Parker's isothermal, transonic solar wind solution (Parker 1958). The velocity of the steady, isothermal solar wind is given by

$$\frac{v^2(r)}{c_s^2}\exp\left(1 - \frac{v^2(r)}{c_s^2}\right) = \frac{r_s^4}{r^4}\exp\left(4 - 4\frac{r_s}{r}\right), \tag{4}$$

where $v(r)$ is the solar wind velocity, $c_s^2 = 2k_{\rm B}T_0/m_p$ is the sound speed, and $r_s = GM_{\odot}m_p/4k_{\rm B}T_0$ is the sonic point. The plasma number density at the base of the atmosphere is a free parameter that we set to 3.6×10^9 cm^{-3} to yield densities of 10^8–10^9 cm^{-3} in the helmet streamer.

Figure 1 shows the spherical wedge domain, for which $R \in [1R_{\odot}, 30R_{\odot}]$, $\theta \in [11.^{\circ}25, 78.^{\circ}75]$, and $\phi \in [-22.^{\circ}5, +22.^{\circ}5]$. By setting our top boundary at $30R_{\odot}$, well above the top of the helmet streamer, we are able to simulate the entire radial extent of the coronal-hole boundary and its transition into the HCS. Shown on the radial surface in Figure 1 is a map of B_r, with green contours drawn to mark the location of the driving (see Section 2.2). Pictured along a slice of constant longitude are the block boundaries, where each block contains $8 \times 8 \times 8$ grid cells. The grid is logarithmically stretched in R. We use an adaptive grid with the highest resolution along the entire coronal-hole boundary and the HCS, as well as a shallow layer of high-resolution cells at the base, to capture the velocity gradients where the solar wind is accelerated and the footpoint driving is imposed. The finest grid at the surface has ~45 points per square degree. The coarsest grids are positioned in the corners of the wedge to save computational resources.

The radial inner boundary is set to be an effusing wall, which allows mass to flow into but not out of the system. Here we also line-tie the magnetic field by setting the tangential velocity everywhere on the surface to zero, except for the prescribed flow profile described below (Section 2.2). The three radial guard cells beneath the lower boundary are held fixed at their initial densities, and their velocities are set to zero. All other boundaries allow mass to flow through, with the density and magnetic fields extrapolated using zero-gradient conditions. The velocities at the radial outer boundary assume free-flow-through (zero gradient) for the normal component and semi-slip conditions (zero value outside the boundary) for the tangential components. At the four side walls, the velocities are set to semi-flow-through (zero value outside) for the normal component and free-slip (zero gradient) for the tangential components. These boundary conditions applied to the initial atmosphere produce a self-sustaining, isothermal solar wind throughout the domain, replenished from below in the open-field regions which have sustained upflows.

As mentioned above, the initial magnetic field (determined from the PFSS solution) and solar wind are not in equilibrium. Consequently, the first part of our simulation is a relaxation phase in which the solar-wind plasma and magnetic field evolve toward a new pressure balance. This relaxed condition is shown in Figure 1, where the thick black magnetic field lines outline the coronal holes at both poles, a stretched helmet streamer at the equator, and a dynamic HCS.

We find that this system never reaches a true time-independent steady state because reconnection continually

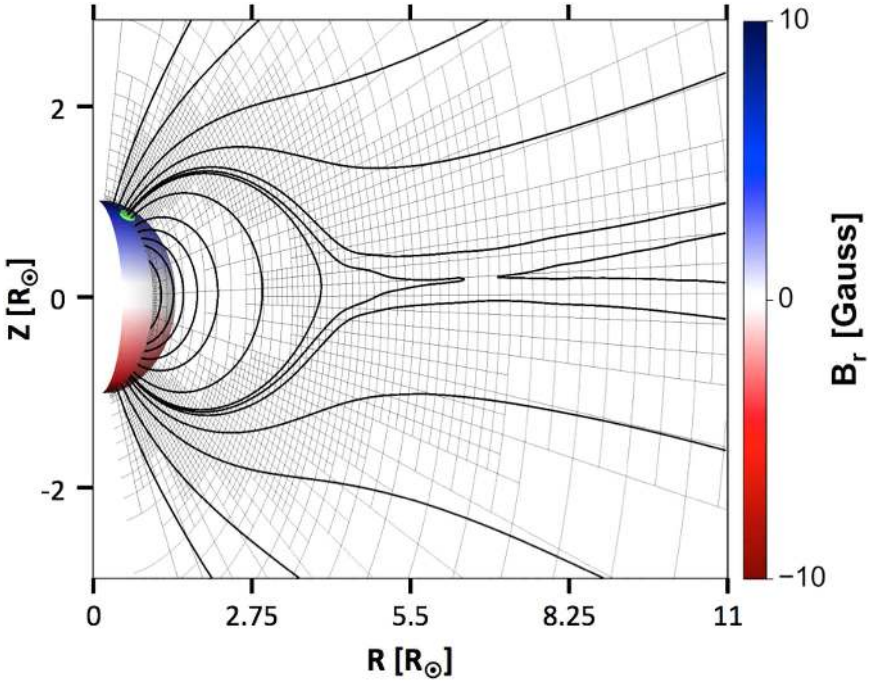

Figure 1. Snapshot of the domain after dynamic relaxation to a quasi-steady state. Grid blocks (thin black lines) are shown in the plane $\phi = 0$. Magnetic field lines (thick black curves) in this plane outline a dipolar magnetic field with two polar coronal holes and a helmet streamer that has recently pinched off at the top near the HCS. The solar surface is color-shaded according to the radial magnetic field component. Green contours in the northern hemisphere show the location of the driving-flow annulus straddling the coronal-hole boundary and are drawn where the tangential velocity magnitude $|\boldsymbol{V}| = 4$ km s^{-1}.

occurs in the HCS near the top of the helmet streamer. Due to the action of the solar wind, which stretches field lines out to infinity, the HCS continuously thins until eventually its width reaches the grid scale. Reconnection at the HCS then forms a flux-rope-like structure that is carried outward with the solar wind. In our simulation, the reconnection is determined by the effective numerical resistivity (i.e., the Lundquist number), which scales directly with the grid spacing. Consequently, the nonsteady dynamics become smaller and occur less frequently as the refinement increases. Scaling our results to solar Lundquist numbers, we expect that the nonsteady background dynamics due to this HCS nonequilibrium reconnection process would have no observable consequences in the imaging data. Thus, this process is not responsible for the formation of the quasi-periodic, slow-wind structures discovered by Viall & Vourlidas (2015) and Kepko et al. (2016). In our simulation, the nonsteady background dynamics merely constitute a very low level of fluctuation above which we easily detect the far larger effects of our surface driving. Moreover, that driving has a fixed scale determined by the size of the observed supergranules and, hence, does not depend upon numerical refinement.

2.2. Boundary Driver

The base dynamics in the heliosphere must be determined by the never-ceasing, supergranular-scale, photospheric convection. The actual photospheric horizontal flows due to supergranules are highly complex, as convective cells appear and disappear randomly throughout the photosphere. Furthermore, the motions have both compressible and incompressible components, with the flows expanding radially from cell centers and converging onto the network, where the misalignment of the flows and their random temporal dependence gives rise to incompressible vortical motions with typical flow speeds of order 1 km s^{-1} (Brandt et al. 1988; Duvall & Gizon 2000; Gizon & Duvall 2003; Komm et al. 2007; Attie et al. 2009; Seligman et al. 2014). For injecting stress into the coronal field, the most important motions are the rotational components. Therefore, for this first investigation of supergranular driving, we use a simple model for a single supergranular flow.

We impose a circular photospheric flow straddling the coronal-hole boundary (the location shown by the green contours on the radial surface in Figure 1). This flow lies in the θ,ϕ plane only and is constructed so as to preserve the normal component of the magnetic field during the evolution. In order to satisfy

$$\frac{\partial B_r}{\partial t} = -\nabla_\perp \cdot (\boldsymbol{v}_\perp B_r) = 0, \tag{5}$$

we choose $\boldsymbol{v}_\perp$ to be equal to the curl of a radial vector,

$$\boldsymbol{v}_\perp = \nabla_\perp \times (\psi, 0, 0). \tag{6}$$

We define ψ as a function of θ, ϕ, and t,

$$\psi(\theta, \phi, t) \equiv V_0 f(t) g(\xi) h(\beta), \tag{7}$$

where

$$f(t) = \frac{1}{2}\left[1 - \cos\left(2\pi k \frac{t - t_0}{t_2 - t_1}\right)\right], \tag{8}$$

$$g(\xi) = \frac{(m + l + 1)}{(l + 1)}[1 - \xi^{2(l+1)}] - [1 - \xi^{2(m+l+1)}], \tag{9}$$

$$h(\beta) = \frac{1}{2}\beta^2. \tag{10}$$

In the equations above, the parameters k, t_0, t_1, and t_2 are set to ramp up the flow to maximum velocity from zero and then

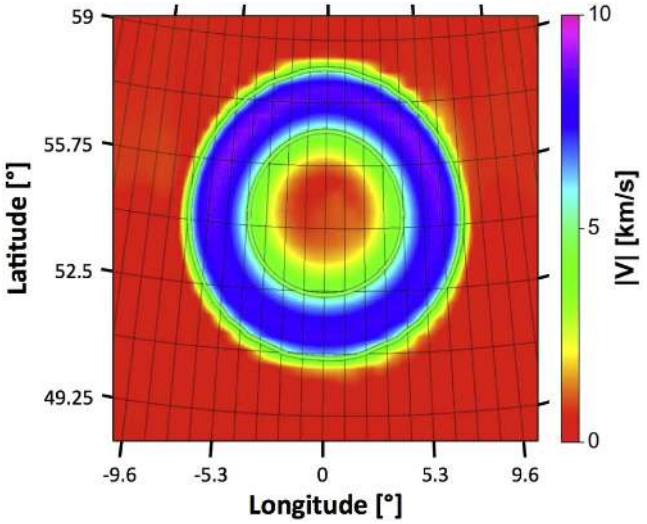

Figure 2. Detail of the bottom radial boundary ($R = 1R_\odot$) showing tangential velocity magnitude at the peak of the driving in color shading. The green contours match the annuli shown in Figure 1. Block boundaries (thin black lines) are also shown.

from that velocity back to zero. This ensures that all disturbances are smooth. The equation for $g(\xi)$ defines an annulus in spatial coordinate ξ, where

$$\xi^2 \equiv 4\left(\frac{\theta - \theta_0}{\theta_2 - \theta_1}\right)^2 + 4\left(\frac{\phi - \phi_0}{\phi_2 - \phi_1}\right)^2. \quad (11)$$

The location of the flow annulus is determined by the limits θ_1, θ_2, and ϕ_1, ϕ_2, with coordinate (θ_0, ϕ_0) representing the center. The thickness and radial velocity profile of the flow annulus are defined by m and l. We set $m = l = 1$ to yield a thick annulus with a velocity peak at the center. In the equation for $h(\beta)$, β is the magnetic field coordinate between minimum and maximum strengths, i.e.,

$$\beta \equiv \max(\min(B_r, B_2), B_1), \quad (12)$$

where we choose $B_1 = 0$ G and $B_2 = 10.0$ G so that $\beta = B_r$ everywhere in our flow region.

A contour map of the tangential velocity on the surface is shown in Figure 2, where the green velocity contours from Figure 1 are shown for context. On the surface, $V_R \approx 0$ so that $|V|$ is essentially the tangential velocity only. The thin black lines show the block boundaries. The flow spans 40×120 grid points and has a diameter of about 1×10^5 km. By comparison, a typical supergranule cell has a diameter of 3×10^4 km (Simon & Leighton 1964).

We adopt the larger size in order to highly resolve the flow on our grid. The cell is centered at 54.°5 above the equator on the coronal-hole boundary and at 0° longitude. The flow extends from 50.°4 to 58.°6, for a total width of 8.°2 in latitude. In longitude, it extends from −7° to +7°, for a total width of 14° in longitude. The parameter V_0 in Equation (7) is chosen so that the maximum flow speed is 9.1 km s^{-1}. We ramp the flow up from zero to this maximum speed, drive it steadily, and then ramp it back down to zero. The maximum speed, 9.1 km s^{-1}, is only 3% of the simulated Alfvén speed on the surface, which is of the same order of magnitude as for the Sun. By placing this flow so that it straddles the coronal-hole boundary, we displace both open and closed magnetic flux from their original equilibrium positions, just as the supergranular flows must distort coronal-hole boundaries on the Sun.

To gain physical insight into the open-closed dynamics, we simulated two cases that are presented below. On the Sun, both the southern and the northern coronal-hole boundaries are driven continuously by random, out-of-phase motions. Our goal, however, is to understand in detail the fundamental dynamics of the boundary. Consequently, we designed the simulations so as to isolate the basic effect of the driving with minimal extraneous complexity. We simulated a large polar coronal hole in order to maximize the effective numerical resolution available to us. However, our results apply to any coronal hole that is larger than the scale of the driver and flanks the helmet streamer, regardless of latitude. As will be evident below, even the simplest driver results in highly complex dynamics. In both cases, we displaced the coronal-hole boundary only in the northern hemisphere using the flow pattern described above. In the first case, we twisted the field-line footpoints through a maximum angle of $\pi/2$, i.e., a quarter rotation. The ramp-up and ramp-down of the driving lasted for 2.4 hr. Afterward, all tangential velocities on the surface were again set to zero, and the system was allowed to relax. This relaxation phase extended to $t = 30.3$ hr. This finite but not extreme distortion of the boundary allows us to examine in detail how the system evolves. In the second case, to better simulate the complexity resulting from constant photospheric driving, we twisted the footpoints through a maximum angle of 2π, i.e., a full rotation. This motion resulted in a very complex distortion of the initial boundary, more like that expected from actual supergranular flow. The driving phase lasted 6.0 hr, and the relaxation phase extended to $t = 75.6$ hr. Below, we present the results of these two simulations.

3. Results

3.1. $\pi/2$ Displacement

Figure 3 shows the imprint of the coronal-hole boundary on the solar surface for the $\pi/2$ rotation at various times during the evolution. Here we show snapshots before driving at $t = -0.0$ hr, immediately after driving at $t = 2.4$ hr, and at three additional times chosen to best illustrate the phases of evolution: $t = 11.6$ hr, $t = 21.0$ hr, and $t = 30.3$ hr. (We strongly encourage the reader to download the full 5-minute-cadence movies that are available online.) At each time, the coronal-hole boundary is shown in both the northern (left) and the southern (right) hemispheres. Only the northern boundary is driven by the rotational flow. In these plots, white represents open magnetic field, and black represents closed. The closed field in the north always connects to the closed field in the south.

To distinguish open and closed fields, we traced a 1000×1818 grid of magnetic field lines distributed over +35° to +75° latitude and −20° to +20° longitude in the north and −75° to −35° latitude and −20° to +20° longitude in the south. Open field is defined as those field lines that reach past $12R_\odot$, where the solar-wind speed becomes greater than the Alfvén speed. At this point, information cannot propagate back to the Sun. Even if a field line "closes" beyond $12R_\odot$, its apex inevitably will be convected outward by the solar wind to the outer domain boundary. Therefore, closed field is defined as

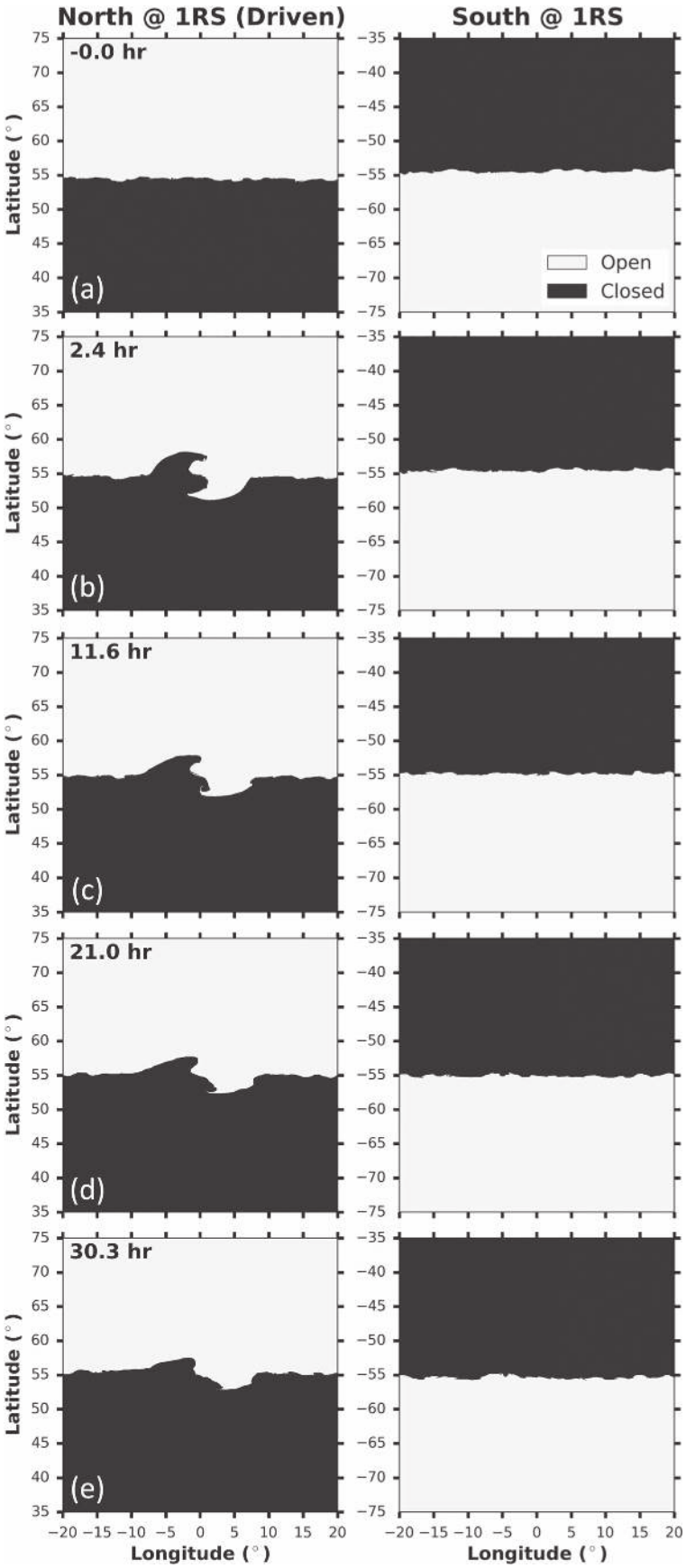

Figure 3. Coronal-hole boundary maps for a peak displacement of $\pi/2$ in the north (left) and south (right). White is open magnetic field and black is closed. (a) Before the driving at $t = -0.0$ hr. (b) End of the driving at $t = 2.4$ hr. (c) $t = 11.6$ hr (d) $t = 21.0$ hr (e) $t = 30.3$ hr. The animation of this figure has a cadence of 5 minutes. (An animation of this figure is available.)

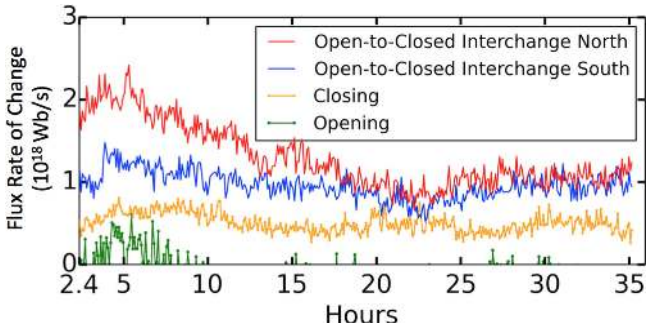

Figure 4. Rate of flux change for a peak displacement of $\pi/2$, where time $t = 2.4$ hr corresponds to the end of the driving. Red and blue lines display the rate of flux change due to interchange reconnection in the north and south, respectively; yellow and green lines display the rate of flux change due to closing and opening, respectively. The rates of opening and closing are identical in the north and south.

those field lines with both footpoints at $1R_\odot$ and apexes that do not reach $12R_\odot$.

As is evident in Figure 3(a), the boundary before driving is mostly undisturbed and roughly straight in both the north and the south, except for the small ripples due to the solar wind and the nonsteady background dynamics at the top of the helmet streamer. In Figure 3(b) the northern boundary has been twisted by the flow (see Section 2.2) by $\pi/2$, whereas the southern boundary, which was not driven, remains undisturbed from its initial state. The twisting caused by the photospheric motion is much larger than any of the ripples in the boundary caused by the nonsteady background dynamics. By simply viewing Figure 3(b), we can conclude that the horizontal, open-closed boundary of Figure 3(a) has been rotated by approximately $\pi/2$. Moreover, the open-closed boundary appears to have undergone almost no relaxation during the 2.4 hr of driving: it simply advects ideally with the photospheric flow. This is a key result with important implications for understanding the open-closed dynamics. The imposed photospheric flows produce a substantial deformation of the northern open-closed separatrix surface very early in the driving and launch nonlinear Alfvén waves in both the open and the closed fluxes. In principle, this could lead to the formation of current sheets and interchange reconnection along the separatrix or open-open reconnection once the wave reaches the HCS above the closed flux. However, we do not see any evidence for such reconnection. The southern coronal-hole boundary appears unchanged between Figures 3(a) and 3(b).

It appears, therefore, that a significant relaxation requires the buildup of a substantial deformation of the closed flux. This result validates our arguments above that only long-timescale photospheric motions, such as supergranular flows, are important for driving the open-closed dynamics. For the parameters of our system, the typical length of the last closed field line is $\sim 10^6$ km, whereas the average Alfvén speed along this flux is $\sim 100\,\mathrm{km\,s^{-1}}$. Thus, the Alfvén travel time is of order a few hours, longer than the 2.4 hr driving time. Consistent with this estimate is the result that, in the simulation, electric currents due to the driving appear at the southern footpoints of the rotated flux 3 hr after the start of the driving. We expect, therefore, that the timescale for the decay of the boundary deformation will be at least 3 hr. Any driving on timescales much shorter than this, such as granules or the magnetic carpet, will only add high-frequency noise to the coronal-hole boundary.

Figure 3 shows this slow decay in detail. Because we do not allow slipping on the photospheric surface after the driving has ended, any change in the coronal-hole boundary is due to (1) the opening of closed field, (2) the closing of open field, or (3) interchange reconnection between the two. The opening of magnetic field lines would register as black changing to white in Figure 3 and corresponds to a closed field line rising up and moving past $R = 12R_\odot$. The closing of magnetic field lines would register as white changing to black and corresponds to two open field lines reconnecting to form a closed field line and a u-loop disconnected field line, which would move with the solar wind and leave through the outer boundary at $30\,R_\odot$. Finally, interchange reconnection would register as either a black-to-white or white-to-black switch and occurs when one open and one closed field line reconnect—most likely in the vicinity of the HCS high in the corona—and switch footpoints. Such an interaction results in the same amount of open and closed flux but changes the connectivity of the system, allowing material that was trapped on the closed field line to move outward into the solar wind. Note that the connectivity shown in all of these plots is instantaneous: any opening of a closed field line shown in the north would also appear immediately as opening in the south.

Figure 3(c) shows the coronal-hole boundaries at $t = 11.6$ hr. By this time, the closed field has had sufficient time to deform substantially in response to the applied photospheric stress. The open-closed boundary in the north shows clear signs of activity, with an intrusion of open field cutting into the closed field near the location of the center of flow. Sharp structure has also appeared on the boundary near the edge of the displaced region around 8° longitude. The southern boundary, in contrast, remains smooth, with no discernible changes.

Figure 3(d) shows the system at $t = 21.0$ hr. At this time, the Alfvén wave on the open field lines has left the system through the outer boundary at $30R_\odot$. The coronal-hole boundary has smoothed out somewhat and is beginning to show clear counterrotation back toward its initial state. Figure 3(e) shows $t = 30.3$ hr, where the southern boundary remains largely unchanged. There is a small distortion near −5° longitude due to the nonsteady background dynamics occurring at the top of the helmet streamer. The coronal-hole boundary in the north, by contrast, has continued to evolve much more dramatically, counterrotating back toward its initial, smooth configuration.

The question now becomes: how is the previously displaced open magnetic field becoming closed and the displaced closed field becoming open? Any true opening or closing of the magnetic field would produce a signature in the south, yet the southern boundary remains largely unaltered. We must conclude, therefore, that interchange reconnection is responsible for the change in the northern boundary. Because this boundary is merely the 2D imprint of a 3D surface that extends well up into the corona and inner heliosphere, the interchange reconnection could be occurring anywhere within or adjacent to that 3D surface.

Figure 4 shows the amount of interchange reconnection experienced by the field lines traced in Figure 3 in the northern (red) and southern (blue) hemispheres, along with the amount of flux closing down (yellow) and opening up (green). Of

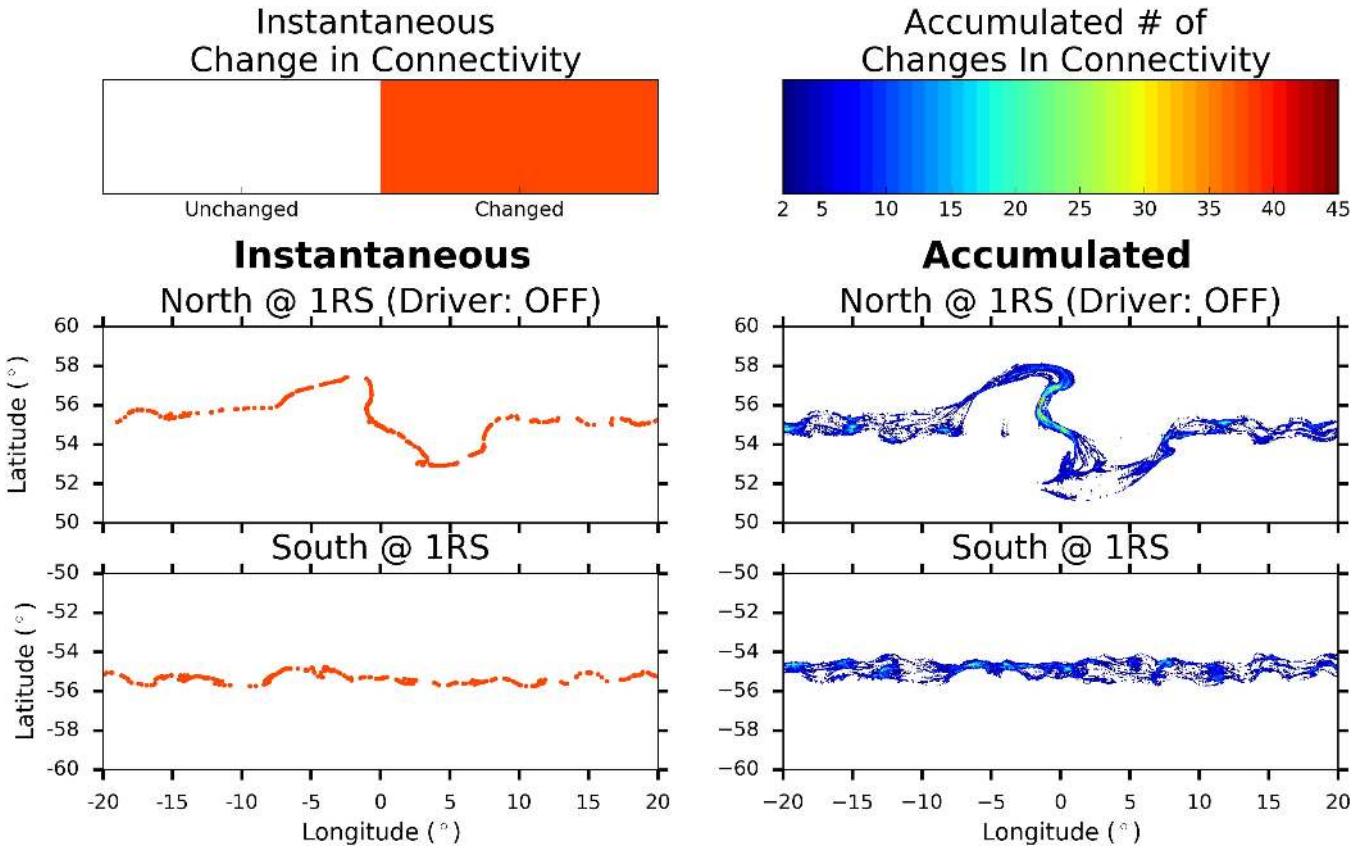

Figure 5. Left: instantaneous change in connectivity in the north (top) and south (bottom) for a peak displacement of $\pi/2$. Red dots indicate the locations of field lines that have changed their connectivity between the previous and current frame. Shown are the final maps at $t = 30.3$ hr. Right: contour plot of the number of times each field line has changed connectivity over the entire duration of the simulation in the north (top) and south (bottom). Field lines that have changed connectivity only once are not shown. The animation of this figure has a cadence of 5 minutes.

(An animation of this figure is available.)

course, the amounts of opening and closing are identical in the two hemispheres, but the interchange can be very different. Figure 4 begins at the end of the driving phase; consequently, any change in connectivity must be due to opening, closing, or reconnection. There is a continual small, but measurable, amount of closing throughout the simulation. This is due to an overall continual closing experienced by the system as it relaxes gradually from its initial PFSS state toward a steady configuration supported by the solar wind. In addition, a quasi-steady amount of interchange reconnection takes place in both hemispheres. This is due to the persistent restructuring of the HCS as a result of the nonsteady background dynamics. Over and above these two processes, a transient enhancement of interchange reconnection occurs principally in the northern hemisphere, where the rate reaches a maximum about 3 hr after the end of the driving phase. This is consistent with our argument above that the relaxation is driven by the deformation of the closed flux and, hence, reflects its intrinsic timescale. The decay time for this interchange is also of order a few hours. There appears to be a rise in interchange reconnection in the south as well, but this is far less clear than in the north. It may well be that the deformation of the closed flux drives the interchange at footpoints that were not driven by the flow.

Our result that interchange reconnection is the dominant relaxation process clarifies why a substantial deformation of the closed flux must build up in order for the relaxation to occur. Interchange reconnection cannot occur if the top of the helmet streamer maintains its classic 2D geometry, with a simple Y-type null and a current sheet only above the closed flux. This region must become strongly 3D, with current sheets forming between the open and closed flux (Wang et al. 2000). Since any stress on the open flux will simply propagate away, it must be the deformation of the closed flux that leads to the current sheets and the ensuing interchange reconnection. A somewhat surprising result is the clear lack of significant field-line opening during the relaxation. There is some weak opening before and during the driving, but this is negligible. A seemingly obvious evolution for relaxing the field would be to open all the stressed closed flux and then simply close down all the flux that is not open in the original, predriven configuration. This would return the system back to its minimum-energy state. In spite of its effectiveness, however, we see no evidence for such evolution. A possible explanation is that closed field lines do expand outward and attempt to open but then encounter open flux and interchange reconnect before reaching $12R_{\odot}$. In any case, our simulation clearly shows that a localized deformation of the open-closed boundary relaxes almost exclusively via interchange reconnection.

To better understand how the interchange is able to produce a global relaxation of the boundary back toward its original shape, we track where it is occurring along the boundary. Figure 5 shows the instantaneous change in connectivity on the left and the accumulated change in connectivity on the right at the final time, $t = 30.3$ hr. (The full movie is available online.) Here again, we are viewing merely the 2D imprint of an extended 3D surface, and the governing interchange dynamics may be occurring anywhere along or very near that surface.

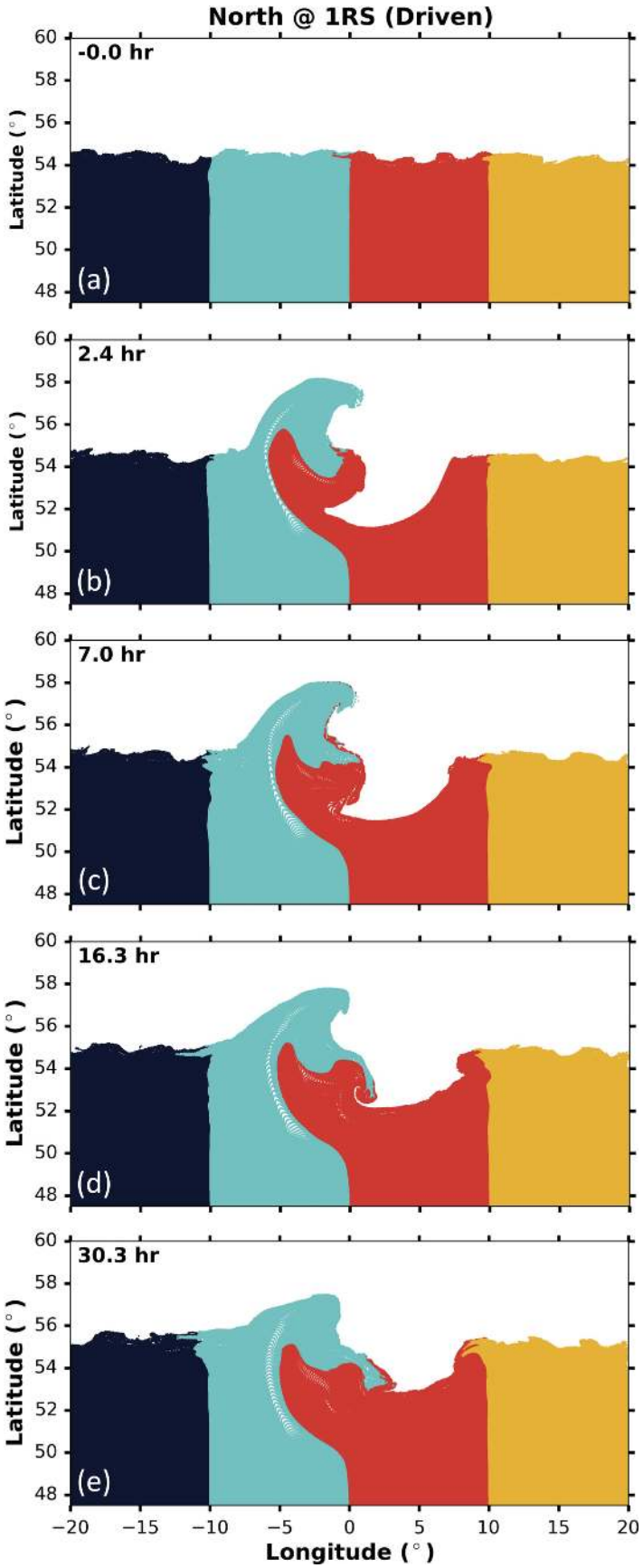

Figure 6. Closed field lines in the north for a peak displacement of $\pi/2$. Field lines are color-shaded based on the longitudes of their conjugate footpoints in the southern hemisphere: navy blue between $-20°$ and $-10°$; teal between $-10°$ and $0°$; red between $0°$ and $+10°$; and yellow between $+10°$ and $+20°$. (a) Before the driving at $t = -0.0$ hr. (b) End of the driving at $t = 2.4$ hr. (c) $t = 7.0$ hr. (d) $t = 16.3$ hr. (e) $t = 30.3$ hr. The animation of this figure has a cadence of 5 minutes. (An animation of this figure is available.)

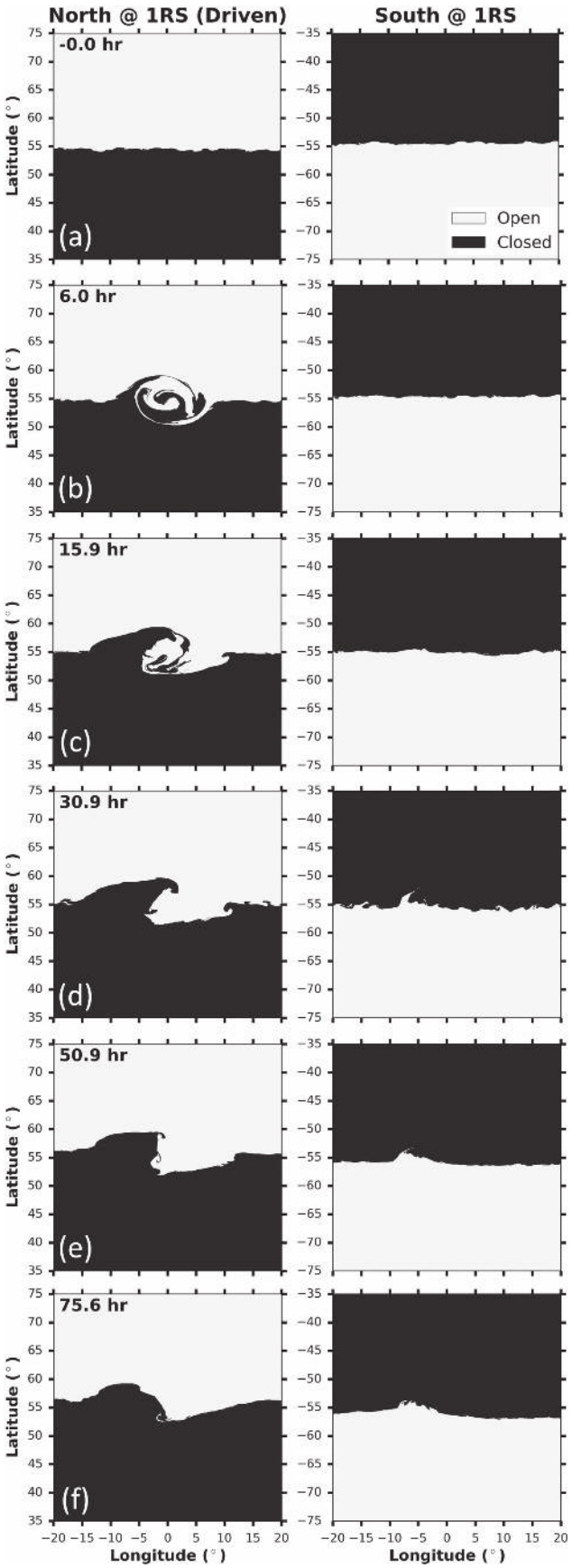

Figure 7. Coronal-hole boundary maps for a peak displacement of 2π in the north (left) and south (right). White is open magnetic field and black is closed. (a) Before the driving at t = −0.0 hr. (b) End of the driving at $t = 6.0$ hr. (c) $t = 15.9$ hr. (d) $t = 30.9$ hr. (e) $t = 50.9$ hr. (f) $t = 75.6$ hr. The animation of this figure has a cadence of 5 minutes.

(An animation of this figure is available.)

The plot on the left showing the instantaneous change is a binary plot, where field lines that changed either from closed to open or from open to closed between the current and previous times are represented by red circles. The right panel shows how many times each field line changed connectivity throughout the simulation, where only field lines that have interchanged twice or more are shown. This means that any change in connectivity due to closing or opening in the overall PFSS relaxation would not be shown.

The movie (available online) shows that, just as in the final frame shown here, there are changes in connectivity all along the coronal-hole boundary from $-20°$ to $+20°$ longitude, even though only the region within $\pm 7°$ was displaced. From the right panel in Figure 5, we can see that many field lines on the boundary interchange more than 5 times, while some field lines in the region near the center of the photospheric rotation interchange over 50 times. This result indicates that interchange reconnection must be the natural response to footpoint stressing and that it must be common in the solar corona and wind.

We find that, through this interchange process occurring everywhere longitudinally along the boundary, locations far from the driven region in longitude are permanently changed. Figure 6 shows the same closed field lines as displayed previously, except that the field lines are colored by the locations of their southern footpoints. Field lines with footpoints between $-20°$ and $-10°$ longitude in the south are navy, those between $-10°$ and $0°$ are teal, those between $0°$ and $+10°$ are red, and those between $+10°$ and $+20°$ are yellow. In the initial field, these also correspond to the location of the northern footpoints, since the field was potential with an axisymmetric mapping from south to north. Figure 6 allows us to clearly observe the change in the global mapping introduced by both the driver and the interchange reconnection. Figures 6(a), 6(b), and 6(c) display the boundary at $t = -0.0$ hr before the driving begins, $t = 2.4$ hr immediately after the driving, and $t = 7.0$ hr, respectively. Figures 6(d) and 6(e) show the late-time maps at $t = 16.3$ hr and $t = 30.3$ hr.

Our driver displaces field lines between $\pm 7°$ longitude (compare Figures 6(a) and 6(b)). However, we see in the other panels of Figure 6 that the field outside of this region is also affected. In Figure 6(c), the boundaries at $\pm 10°$ have already begun to change, and still larger changes are evident in Figures 6(d) and 6(e). Most importantly, we see in Figure 6(e) that the closed, teal-shaded flux that was the most displaced between $-5°$ and $0°$ has migrated down and pushed out the closed-field boundary between $-13°$ and $-7°$. We also see that the yellow flux from beyond $+10°$ has been displaced into the initially red region, even though this flux was not driven.

It is evident by comparing Figure 6(a) to Figure 6(e) that the system cannot return to its original state even if allowed to relax indefinitely. Figure 4 shows that the amount of reconnection occurring at the end of the simulation has leveled off. Consequently, we conclude that by $t = 30.3$ hr the system has reached a new quasi-steady state. This state differs from the original primarily in the presence of twist deep within the closed-field region. Since this twist is large-scale and far from the open-closed boundary, it does not produce any current sheets and cannot relax via reconnection. Even if reconnection could easily occur in the closed region, it could not return the field to its original, unstressed state due to helicity conservation (e.g., Taylor 1974, 1986; Antiochos 2013). Of course, on the Sun, a coronal-hole boundary never relaxes to some unperturbed state because it is being driven continuously by the random supergranular flows. The key conclusion from the results presented here is that the timescale for full relaxation via interchange reconnection is of order 10 hr or so, which is comparable to the driving time. Therefore, solar coronal-hole boundaries are never quasi-steady but rather are strongly dynamic.

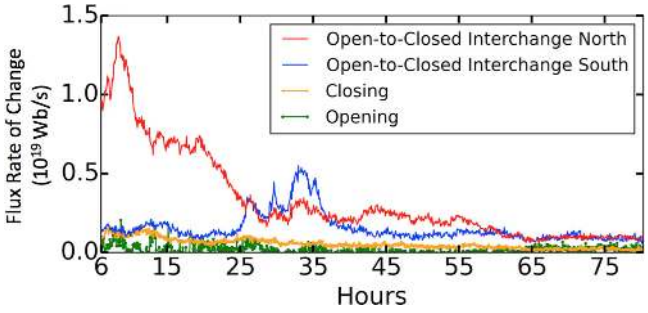

Figure 8. Rate of flux change for a peak displacement of 2π, where time $t = 6.0$ hr corresponds to the end of the driving. Red and blue lines display the rate of flux change due to interchange reconnection in the north and south, respectively; yellow and green lines display the rate of flux change due to closing and opening, respectively. The rates of opening and closing are identical in the north and south.

3.2. 2π Displacement

In order to determine the coronal-hole boundary dynamics for a strong, continuous driver, we performed and analyzed a simulation with a full 2π rotation, corresponding to the complete lifetime of a supergranule. We kept the maximum velocity the same as in the $\pi/2$ case and drove the system at this steady rate for a longer duration in order to reach the specified displacement. Because the top of the helmet streamer becomes much more distorted in this case, the results presented below exhibit much more drastic dynamics than those above. On the Sun, convective cells continuously appear and disappear randomly on the photosphere. The results presented below, therefore, still represent a great simplification from the true complexity of solar coronal-hole boundary dynamics.

Figure 7 shows the coronal-hole boundary throughout the rotation. As in Figure 3 the open field is represented by white and closed field by black, with the northern hemisphere shown on the left and the southern on the right. Figure 7(a) shows the boundaries before the onset of driving at $t = -0.0$ hr, and Figure 7(b) shows the boundaries immediately after the driving has ceased at $t = 6.0$ hr. The grid has sufficiently resolved one complete rotation of the coronal-hole boundary. While the boundary is strongly twisted in the north, there have been no changes to the southern boundary even though there has been sufficient time for the stress to propagate to the southern footpoints. Note that the full 2π rotation induces an extreme deformation of the boundary, yielding much more fine structure than the $\pi/2$ case above. This is the reason for first analyzing and gaining insight from the case with a small rotation. Observe also that the structure of the boundary at $t = 6.0$ hr is not due solely to ideal convection. There must have been considerable reconnection to form the detailed small-scale structure visible at the end of the driving phase. This is to be expected, given our finding above that the timescale for relaxation is 3 hr or so.

In light of this fine-scale structuring, it may seem surprising that even with the extreme deformation of the northern

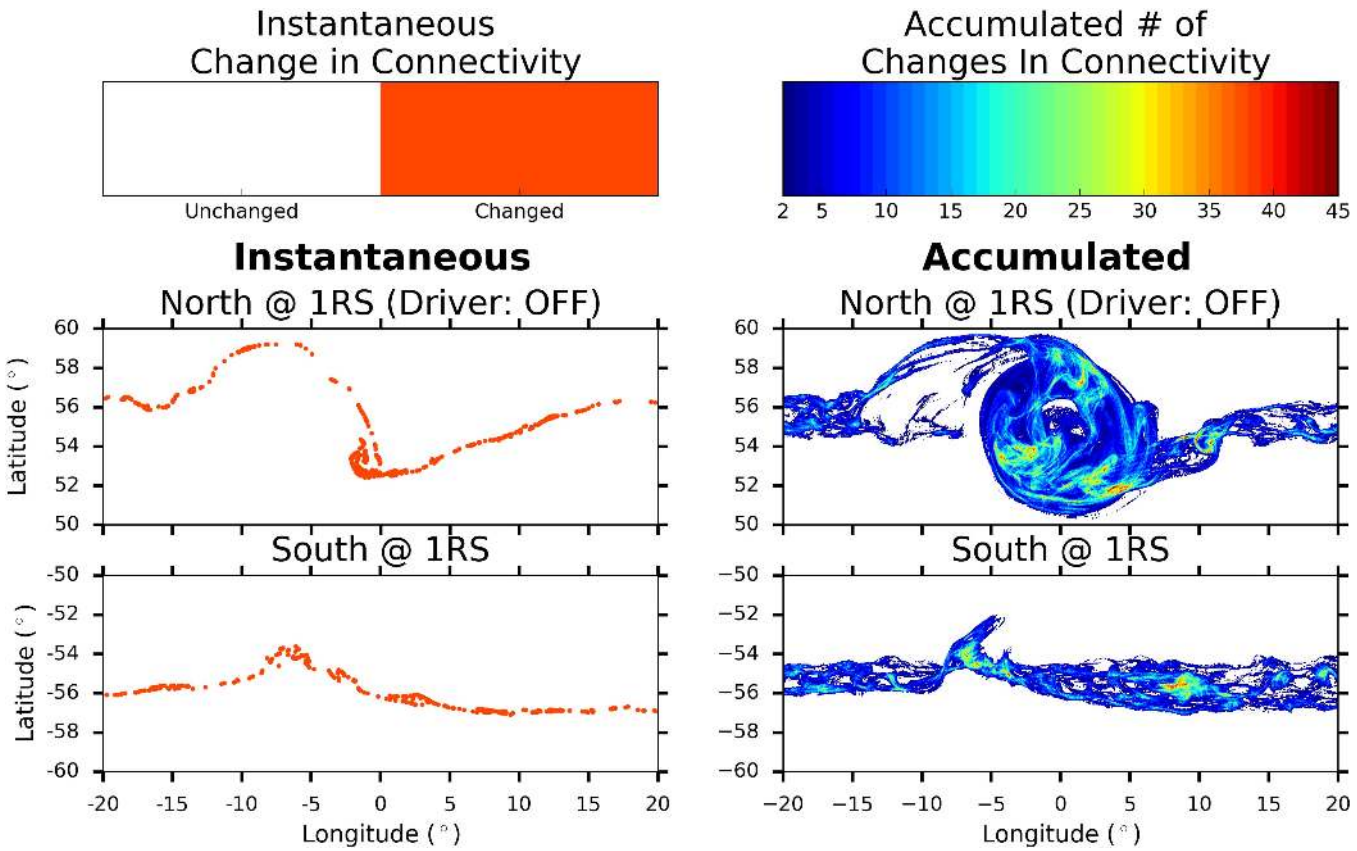

Figure 9. Left: instantaneous change in connectivity in the north (top) and south (bottom) for a peak displacement of 2π. Red dots indicate the locations of field lines that have changed their connectivity between the previous and current frame. Shown are the final maps at $t = 75.6$ hr. Right: contour plot of the number of times each field line has changed connectivity over the entire duration of the simulation in the north (top) and south (bottom). Field lines that have changed connectivity only once are not shown. The animation of this figure has a cadence of 5 minutes.

(An animation of this figure is available.)

boundary, there is no observable effect on the southern. One reason for this result is that, on the timescale of 6 hr, any change in the south could only be due to interchange or closing. As noted previously, we define a field line to be open if it intersects the $R = 12R_{\odot}$ surface. Since it takes approximately 12 hr or so in our simulation for a disturbance, whether mass flow or Alfvén wave, to propagate out to this surface, no opening can occur until later. The closing of field lines could, in principle, occur on the timescale of 6 hr, but this is unlikely given that the addition of large magnetic stress into the corona should result in a net opening of flux rather than closing. Furthermore, it is unlikely that a large amount of interchange would occur in the south, because this would only deform the boundary away from its initial quasi-steady position.

Figure 7(c) shows the boundary at $t = 15.9$ hr, while Figures 7(d), 7(e), and 7(f) show the boundaries at $t = 30.9$ hr, $t = 50.9$ hr, and $t = 75.6$ hr. These frames were chosen to best illustrate the phases of evolution. At early times, comparing $t = 6.0$ hr and $t = 15.9$ hr, we observe rapid evolution in the regions that are displaced the most. The movie available online shows the development and decay of fine-scale structure at the northern boundary throughout this process, just as in the $\pi/2$ case. Notice, however, that the evolution sometimes demonstrates the development of very fine corridors of both open and closed flux, but these corridors eventually disappear. The southern boundary, in contrast, remains unchanged during this time, despite the extreme dynamics in the north. By $t = 30.9$ hr, the changes in the north have slowed as the finest-scale structure has been interchanged away. We continue to see slow changes in the northern hemisphere along the lines of the behavior of the $\pi/2$ case. However, now the southern boundary has begun to show changes. Note in particular the spike-like indentation of open flux into the southern closed-field region. This feature could be due to the opening of flux that has reached the 12 $R_{\odot}$ surface, but we will show below that it is due to interchange. Additionally, we see a distinct corrugation of both the northern and the southern boundaries. This is due to localized opening or closing of flux, which occurs on a smaller scale even without the driving, but here it is enhanced by the induced stresses. The corrugation disappears over the next 10 hr or so. By the end of the simulation, which is nearly 3 days after the driving has stopped, the northern coronal-hole boundary has nearly—but not quite—returned to its initial state. The only significant change in the south, meanwhile, is that the spike of open flux has broadened into a smooth indentation, indicating that there has been a localized opening due to the stress that now resides permanently in the closed-field region.

Figure 8 shows the amount of interchange reconnection, closing, and opening that these field lines experience after the end of the driving, just as in Figure 4. As before, the red and blue lines indicate interchange reconnection in the north and south, respectively, and the yellow and green lines show the amount of closing and opening, respectively. Before the onset of driving, the amounts of interchange reconnection in the north and south match those found in the $\pi/2$ case. As the driving ceases, however, the interchange in the north increases rapidly, reaching a maximum rate approximately 3 hr after the end of the driving.

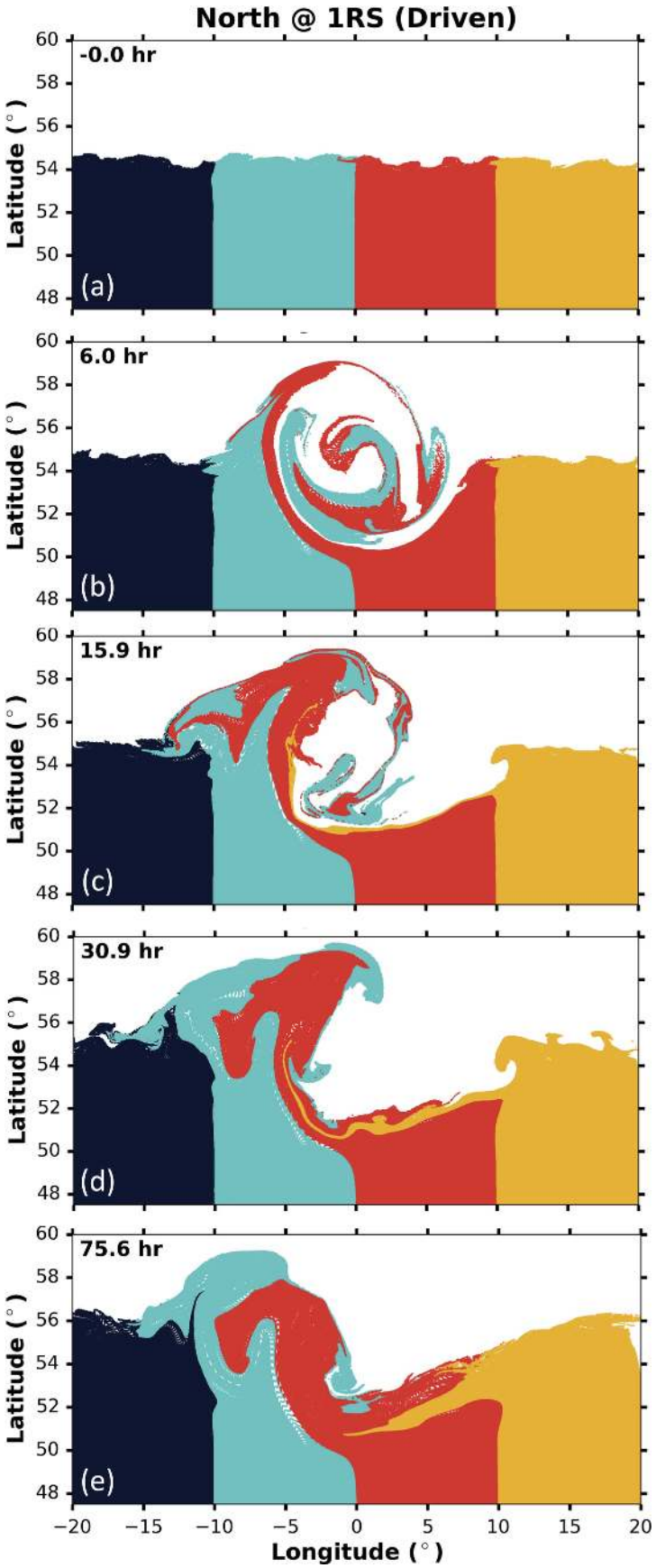

Figure 10. Closed field lines in the north for a peak displacement of 2π. Field lines are color-shaded based on the longitudes of their conjugate footpoints in the southern hemisphere: navy blue between $-20°$ and $-10°$; teal between $-10°$ and $0°$; red between $0°$ and $+10°$; and yellow between $+10°$ and $+20°$. (a) Before the driving at $t = -0.0$ hr. (b) End of the driving at $t = 6.0$ hr. (c) $t = 15.9$ hr. (d) $t = 30.9$ hr. (e) $t = 75.6$ hr. The animation of this figure has a cadence of 5 minutes.

(An animation of this figure is available.)

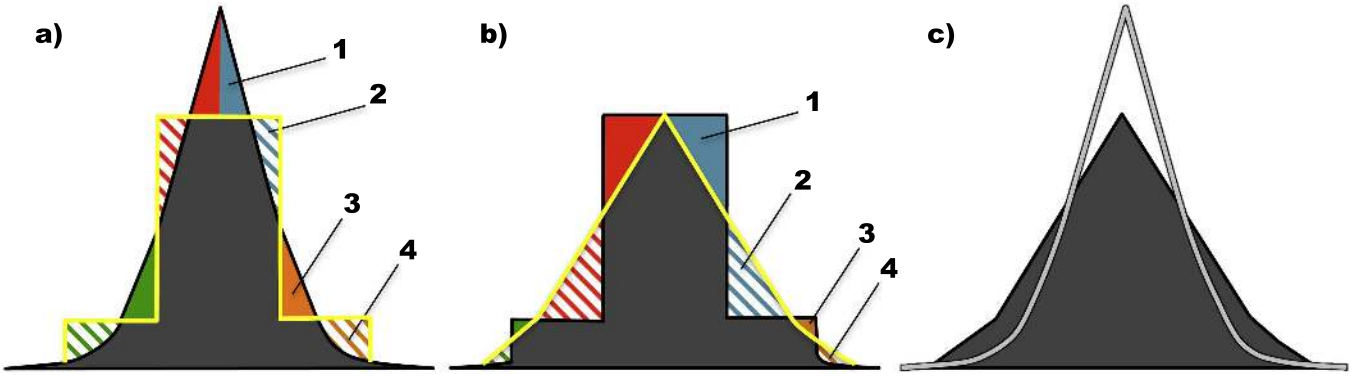

Figure 11. Cartoon schematic of interchange reconnection changing the boundary of a closed-field region. Solid black line: old coronal-hole boundary. Yellow line: new coronal-hole boundary. Gray line: original coronal-hole boundary. Solid-shaded gray, red, blue, green, and orange areas represent closed-field regions. Striped red, blue, green, and orange areas represent open-field regions. Panels (a), (b), and (c) illustrate the evolution over time as closed regions 1 and 3 experience interchange reconnection with open regions 2 and 4, respectively. See the text for details.

This timescale is the same as that found in the $\pi/2$ case, but the amplitude is 6 times larger here for the larger displacement. As before, there is no noticeable increase in the interchange rate in the south, at least on the scale of the figure.

The interchange in the south subsequently shows a broad rise and attains a maximum, but only about 20 hr after the end of the driving. In fact, the interchange rate in the south surpasses that in the north during this period. Notice that after about 40 hr or so, the interchange in the north again rises and eventually surpasses that in the south. It appears that there is a global oscillation in the interaction between the open and closed flux during this relaxation. The stress in the closed field propagates quickly, at the Alfvén speed, and for a force-free field should equilibrate along field lines. We expect, therefore, that after 10 hr or so, the closed flux will reach an equilibrium. At first, this equilibrium produces current sheets in the open flux only in the north, which has been deformed by the flow. The relaxation in the north by interchange is sufficiently fast, however, that eventually it throws the south out of balance. The south then begins to interchange rapidly as well and surpasses the interchange occurring in the north. This exchange occurs once more before the two rates decline to become almost identical by $t = 65$ hr. Although interesting, this oscillation is not relevant to the Sun, where both the northern and the southern boundaries would be driven simultaneously and continuously. It does, however, emphasize the 3D nature of the dynamics. It also hints that the location experiencing interchange reconnection is more likely to be near the top of the helmet streamer than close to the solar surface, as this location migrates over time from the northern to the southern hemisphere and back again. We discuss the radial location of the interchange reconnection in more detail in Section 4.

Figure 9 is the final frame of the movie available online, which shows the instantaneous and accumulated changes in connectivity due principally to interchange reconnection. The left panel shows that, as before, interchange reconnection is occurring at all longitudes along the entire coronal-hole boundary. The right panel shows that hot spots of connectivity changes exist in regions with the most structure, and that individual field lines interchange over 50 times, as observed earlier. Note that even in the south, where there is no photospheric driving, some locations show numerous interchanges taking place.

The long-term effect of this large amount of interchange on its surroundings is shown in Figure 10 in the same style as Figure 6.

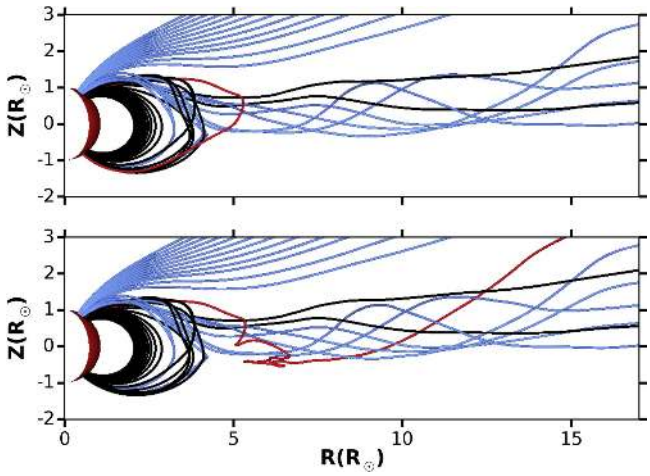

Figure 12. Example of an individual interchange event from the 2π displacement case. Blue field lines were originally open; black field lines were originally closed. The red field line interchange-reconnects from closed to open between the top and bottom panels, which are 5 minutes apart. See the text for details.

Closed field lines are grouped into four regions based on the locations of their southern footpoints. Figure 10(a) shows the coronal-hole boundary and closed-field region before the driving begins at $t = -0.0$ hr, Figure 10(b) shows them immediately after driving at $t = 6.0$ hr, and Figure 10(c) shows them at $t = 15.9$ hr. Figures 10(d) and 10(e) show late-time snapshots at $t = 30.9$ hr and $t = 75.6$ hr, respectively. (The full movie is available online.)

The interchange reconnection works quickly at the beginning. At $t = 15.9$ hr (Figure 10(c)), field lines in the teal and red regions that were displaced can already be seen cascading along the boundary toward $-10°$ longitude. In Figure 10(d), the interchange continues to push the boundary north around $-10°$ longitude. Also, a teal-shaded finger extends all the way to $-15°$ longitude, 6° beyond the initial flow region, while field lines from the yellow-shaded region beyond $+10°$ longitude have interchanged their way along a large portion of the boundary, despite not having been driven. Notice also that there is clear evidence for reconnection within the closed-field region. A long yellow-shaded filament, which at one time extended far into the red region, retracts considerably back toward its original location. Figure 10(e) at $t = 75.6$ hr, nearly 3 days after the end of the

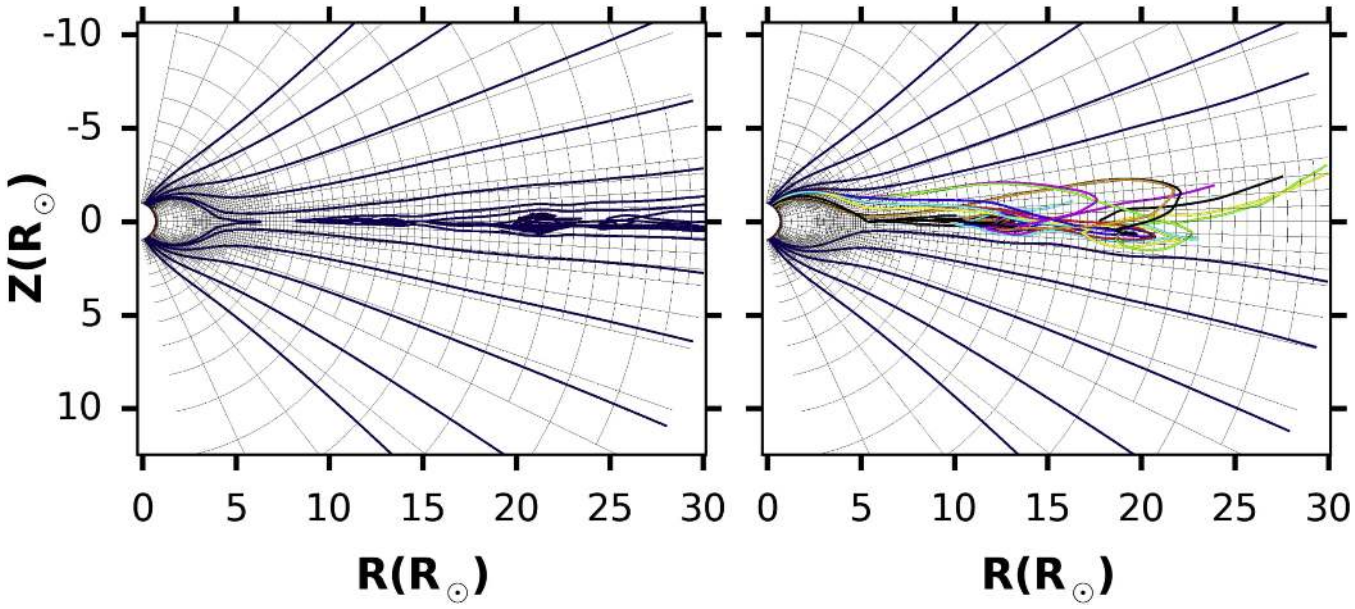

Figure 13. Change in width of the dynamic slow-wind region for the 2π displacement case. Left: Blue field lines in dynamic equilibrium show a narrow, $\sim 5^{\circ}$ width of the slow solar wind. Right: Multicolored field lines extend to much higher latitudes due to interchange reconnection driven by the photospheric flow, showing a broad, $\sim 15^{\circ}$ width of the slow solar wind.

driving, shows that even though the boundary may appear smooth and close to its original configuration, the closed-field region remains quite far from its initial state. Of course, any such structure would not survive long on the Sun, because subsequent photospheric rotations would completely destroy it.

4. Discussion

The key result of our simulations is that interchange reconnection dominates the evolution of the open-closed boundary when driven by a photospheric rotation. Although some flux opening and closing does occur, it is far outweighed by interchange. As discussed above, this is somewhat unexpected, because flux opening is generally assumed to be the mechanism by which the corona sheds magnetic stress, certainly the large-scale magnetic shear evident in coronal mass ejections (e.g., Lynch et al. 2016). Interchange reconnection is typically not expected to produce marked changes in coronal-hole boundaries, since interchange at any arbitrary location along a perturbed boundary is not guaranteed to help the boundary evolve back toward its lowest-energy state. In Figure 3 interchange would show up as a switching of a black and a white point, so if this occurs across the boundary at the point of maximum displacement, the interchange actually could move the system farther from its preferred state. Instead, the tip of the displaced closed-field region interchanges with field lines along the boundary in a manner that broadens the closed-field region but smoothes the boundary. The result is displaced field lines pushing along the coronal-hole boundary in a manner that makes the zone of maximum displacement appear to be diffusing back into the closed-field region. This effect can be seen in Figures 6(d) and 6(e), where the teal-shaded region of field lines is pushing into the navy and red regions.

The key to understanding this evolution is that interchange reconnection usually acts to smooth out any sharp structure that forms along the boundary. We emphasize, however, that interchange does not always smooth out structure. The movies of the 2π case clearly show the transient formation of long, thin filaments of both closed and open field during the relaxation. Furthermore, the southern boundary often builds up fine-scale structure, even though this boundary was not driven. The structures due to interchange are fairly short-lived, but they do show that interchange cannot be thought of as a purely diffusive process. For the most part, however, interchange reconnection evolves the entire boundary, not just where the displacement occurs, so as to smooth out any sharp features. Our simulations show that localized photospheric driving produces a permanent change in the open-closed boundary, even far from the driven region.

A heuristic picture of the effects of interchange reconnection is shown in Figure 11. Panels a, b, and c illustrate how the coronal-hole boundary (solid black line) changes with time. The closed-field region is represented by the solid-shaded gray, red, blue, orange, and green areas beneath the solid black line. The striped regions above the solid black line are open-field regions. Between panels a and b, interchange reconnection occurs between the closed-field region 1 and open-field region 2 and between the closed-field region 3 and open-field region 4. The pattern repeats on the left side, with like-colored regions interchanging. The new boundary that results from this interchange is shown as the yellow line in panel a and becomes the new coronal-hole boundary shown in black in panel b. The process then continues, resulting in the black coronal-hole boundary shown in panel c. The original boundary is shown in gray, over the top of the new one in black, in panel c. The overall effect is to shrink the height of the region while broadening it and preserving its area. A large fraction (though not all) of the evolution seen in our simulations is simply the cumulative effect of this process.

Two important aspects of the evolution of our system are implied by Figure 11 but may not be immediately apparent. First, if we were to repeat the process shown in panels a and b on the black triangle of panel c, then a section of the closed-field region farther down along each side, which

was previously open, would reopen. Some of this section could close again in a subsequent set of interchanges. This explains the result of Figure 9(a), which shows that some locations undergo numerous interchange reconnections. Second, note that the center of photospheric rotation is likely to be a location of many interchanges. The interchange process illustrated in Figure 11, occurring around the center of the boundary deformation for the $\pi/2$ case of Figure 3, would act very much like a counterrotation of the boundary. It is especially advantageous for interchange to occur here and, thereby, to bring the system back to its original state. Figure 5 demonstrates that, in fact, interchange occurs around this location over 50 times in 30 hr.

Figure 12 presents an example of interchange reconnection that occurs within our system at approximately $t = 13$ hr. It shows a set of field lines drawn from fixed locations in the northern hemisphere at two different times, 5 minutes apart, during the 2π simulation. The field line in red is traced from exactly the same location in both images. In the top panel, the red field line is closed, and in the bottom, it is open. The interchange-reconnection point is at the sharp kink shown in the bottom panel, separating the old part of the field line, which obviously has not changed as it is traced back toward the Sun, from the new part of the field line with its open end. This kink verifies that the interchange reconnection is occurring principally at the top of the helmet streamer. The fact that the interchange takes place near the streamer top is not surprising because, for a force-free field, any magnetic twist or stress is expected to propagate to the region of weakest field (Parker 1979). In our case, this corresponds to the top of the helmet streamer. It also happens to be the location of a preexisting current sheet, the HCS, enabling the formation and enhancement of current sheets. Plasma distributed along the field line from the point of the kink down to the surface is now free to flow outward into the solar wind after residing in the hot corona on a closed field line.

Our result that a single field line can interchange over 50 times implies that a spacecraft sampling along a single field line could, in fact, sample plasma from regions that are remote from each other on the Sun. This would have the effect of spreading plasma from closed field lines out into the heliosphere, with the interchange reconnection acting as a kind of diffusion. The S-Web model (Antiochos et al. 2011) predicts that photospheric motions will broaden the regions where reconnection is likely to occur and increase the width of the source regions of slow solar wind in the heliosphere. Figure 13 shows the width of the dynamic slow-wind region in our simulation along the HCS. On the left, at time $t = -0.0$ hr, line-tied field lines exhibit the dipolar shape of the magnetic structure before the onset of driving, while field lines plotted within the HCS show the tangled magnetic fields that are released by the pinching off of the helmet streamer and convected out with the solar wind. In our case, the dynamic region near the HCS results from the nonsteady background fluctuations due to numerical reconnection, so that the width of this dynamic region is determined by the grid. On the right, at time $t = 29.9$ hr, the same blue line-tied field lines are plotted along with open field lines traced from within the flow region on the surface. Whereas on the left, the dynamic region consists only of a narrow, 5°-wide region due to the nonsteady background dynamics, on the right, the width of the dynamic region is much broader: about 15°. Open field lines within this region trace outward as far as 15°, but they also wrap into the HCS, mixing plasma from these two very different sources.

5. Conclusions

The simulations presented in this paper reveal several important new properties of the open-closed field boundary in the solar corona and heliosphere. The first is that, on the Sun, the magnetic field near this boundary responds to photospheric driving primarily via interchange reconnection near the top of the helmet streamer. This result holds for the flows that are likely to be the most important drivers of the boundary: the quasi-random twisting and shearing, on timescales of a day or so, induced by the ever-present supergranular convection. Although we certainly see closed flux opening and open flux closing in our simulations, these processes are minor compared to the interchange reconnection. In fact, since interchange reconnection is so efficient, we expect it to also dominate the coronal-hole boundary evolution due to other driving motions, such as differential rotation or meridional flow, which have much larger spatial and temporal scales. This result holds not only for more complex driving motions but also for a more complex coronal-hole boundary. All that is required is for the coronal hole to be significantly larger than the scale of the driver and for it to be adjacent to a helmet streamer, thus connecting it directly to the HCS.

We conjecture that interchange will always dominate if the photospheric driving is fully 3D and involves mainly the displacement of existing photospheric flux, rather than a change in the amount of flux. If a large amount of new flux emerges so that the total unsigned flux at the photosphere increases significantly, then we expect that the amount of open flux will increase as well. Flux emergence, therefore, will result in closed flux opening, although there may also be some interchange. Conversely, photospheric flux disappearance will result in open flux closing. Large changes in the amount of photospheric flux, however, occur on the timescale of the solar cycle, of order years, whereas the timescale for flux evolution due to supergranular motions is only of order a day. We conclude, therefore, that interchange reconnection almost always dominates the dynamics at coronal-hole boundaries.

Another important finding from our simulations is that the timescale for boundary relaxation by interchange reconnection is commensurate with supergranular driving. It is evident from our 2π case that, at an average speed of $\sim 9\,\mathrm{km\,s^{-1}}$, the photospheric motion induces a strong, nearly ideal deformation of the coronal-hole boundary. Some relaxation occurred over the 6 hr duration of our driver, but the interchange dynamics peaked several hours after the end of the driving and were significant for at least 30 hr. If we were to reduce the driver speed by a factor of 5, so as to more closely match the solar photosphere, we expect that the boundary deformation would be smaller, but there would still be a pronounced deformation of the boundary and copious interchange reconnection. A possible caveat to this conclusion is that the effective Lundquist number for our simulation, which we estimate to be $\sim 10^4$, is orders of magnitude smaller than the actual solar value, $\sim 10^{12}$. In principle, this could result in much slower reconnection than is produced by our simulation and, thereby, alter the balance between interchange versus opening and closing. However, there are compelling arguments against this possibility. A key point is that our system has a large-scale separatrix surface, the open-closed boundary, with a null line and an initial current

sheet, the HCS. A large number of simulations, by ourselves and many others, of systems with such preexisting separatrices and null points show that stressing such topologies leads to the formation of current sheets at the separatrices on ideal-MHD timescales (Priest & Forbes 2000). Furthermore, the rate of interchange reconnection need not be fast but must merely keep pace with the slow photospheric driving. In our simulations, the reconnection rate is of order a few percent of the Alfvén speed, and there is no evidence of explosive reconnection. We expect, therefore, that on the Sun, where the driving is continuous and slow, the interchange reconnection would achieve a quasi-steady balance with the photospheric motions (e.g., Edmondson et al. 2010b).

Our results also have important implications for understanding the topology of the open and closed flux in the corona. Careful examination of the movie for the 2π case reveals that, in spite of the extremely fine structure that develops during the evolution, both the closed- and open-flux regions remain simply connected. There is no evidence for disconnected open-flux patches within the closed-field region, even though the system is fully dynamic and includes numerous current sheets. This agrees with other simulations of coronal-hole boundary evolution (Edmondson et al. 2010a; Linker et al. 2011) and supports the coronal-hole uniqueness hypothesis of Antiochos et al. (2007). This result also provides indirect support for the S-Web model for slow-wind origin (Antiochos et al. 2011), in contrast to the interchange model of Fisk and coworkers, which postulates that open flux can diffuse throughout the closed-field region (Fisk et al. 1998; Fisk 2003).

For understanding in situ measurements of the slow wind, the most important conclusion from our simulations is that the magnetic flux near the open-closed boundary is constantly undergoing cycles of opening and closing via interchange near the inner edge of the HCS on timescales of approximately 30 hr. This implies that closed-loop plasma that has been in the corona for a day or more is continuously being released into the solar wind. Such plasma could well explain the observed characteristics of the slow wind, a charge-state abundance indicative of the closed corona, and significant FIP enhancements (Zurbuchen 2007). We emphasize that the timescale of 30 hr is critical because it takes roughly a day for coronal loops to build up an elemental abundance that differs significantly from the photosphere (Feldman & Widing 2002). Our results can also explain the observation that most of the slow wind does not exhibit bidirectional heat fluxes, which are evidence of flux opening, or heat-flux dropouts, which are evidence of flux closing (Gosling 1990; Lin & Kahler 1992). For remote-sensing observations of the corona, our calculations predict that the boundaries of coronal holes should have a highly irregular structure on scales considerably smaller than supergranules and should exhibit a slow, quasi-cyclic evolution. It may be possible to identify such an evolution from high-resolution images of coronal holes.

It must be noted, however, that the Sun exhibits several features that are not included in our simulations and are likely to have strong effects on any observations of the corona and wind. In particular, the photosphere displays persistent emergence and cancellation of magnetic flux at both small and large scales. We expect this to drive systematic evolution of coronal-hole boundaries, including large-scale opening and closing, while small-scale emergence/cancellation will produce a constant background of brightening and dimming in coronal images. Even more important, the flux distribution at the photosphere is never that of a simple dipole. As a result, the distribution of coronal holes is almost never that of two simple polar holes, as in our simulation. The coronal-hole structure as inferred by either source-surface or MHD models (Titov et al. 2011) generally is intricately organized, with multiple coronal-hole extensions reaching low solar latitudes. According to the S-Web model, such a complex coronal-hole topology is essential for understanding the observations that the slow wind can be found far from the HCS (Antiochos et al. 2007, 2011). Future simulations with much higher numerical resolution will be required to understand the dynamical response of such a complex open-closed boundary to photospheric driving and to determine whether the ensuing dynamics can explain the slow solar wind.

AKH, SKA, and CRD were supported by the NASA Living with a Star and Heliophysics Supporting Research programs. PFW acknowledges support from the NASA Postdoctoral Program at GSFC. The large, lengthy numerical simulations performed and analyzed in this paper were supported by grants of NASA High-End Computing resources to CRD and were carried out on the Discover cluster at NASA's Center for Climate Simulation.

References

Altschuler, M. D., & Newkirk, G. 1969, SoPh, 9, 131
Antiochos, S. K. 2013, ApJ, 772, 72
Antiochos, S. K., DeVore, C. R., Karpen, J. T., & Mikić, Z. 2007, ApJ, 671, 936
Antiochos, S. K., Mikić, Z., Titov, V. S., Lionello, R., & Linker, J. A. 2011, ApJ, 731, 112
Attie, R., Innes, D. E., & Potts, H. E. 2009, A&A, 493, L13
Brandt, P. N., Scharmer, G. B., Ferguson, S., Shine, R. A., & Tarbell, T. D. 1988, Natur, 335, 238
Burlaga, L. F., Ness, N. F., Wang, Y.-M., & Sheeley, N. R. 2002, JGRA, 107, 1410
Crooker, N. U., Gosling, J. T., & Kahler, S. W. 2002, JGRA, 107, 1028
Del Zanna, G., & Bromage, B. J. I. 1999, JGRA, 104, 9753
DeVore, C. R. 1991, JCoPh, 92, 142
Doschek, G. A., & Feldman, U. 1977, ApJL, 212, L143
Doschek, G. A., Warren, H. P., Laming, J. M., et al. 1997, ApJL, 482, L109
Druckmüller, M. 2009, ApJ, 706, 1605
Duvall, T. L., Jr., & Gizon, L. 2000, SoPh, 192, 177
Edmondson, J. K., Antiochos, S. K., DeVore, C. R., Lynch, B. J., & Zurbuchen, T. H. 2010a, ApJ, 714, 517
Edmondson, J. K., Antiochos, S. K., DeVore, C. R., & Zurbuchen, T. H. 2010b, ApJ, 718, 72
Endeve, E., Holzer, T. E., & Leer, E. 2004, ApJ, 603, 307
Feldman, U., Doschek, G. A., Mariska, J. T., Bhatia, A. K., & Mason, H. E. 1978, ApJ, 226, 674
Feldman, U., & Widing, K. G. 2002, PhPl, 9, 629
Feldman, U., & Widing, K. G. 2003, SSRv, 107, 665
Fisk, L. A. 2003, JGRA, 108, 1157
Fisk, L. A., Schwadron, N. A., & Zurbuchen, T. H. 1998, SSRv, 86, 51
Fisk, L. A., & Zhao, L. 2009, in IAU Symp. 257, Universal Heliophysical Processes, ed. N. Gopalswamy & D. F. Webb (Cambridge: Cambridge Univ. Press), 109
Fisk, L. A., Zurbuchen, T. H., & Schwadron, N. A. 1999, ApJ, 521, 868
Geiss, J., Gloeckler, G., von Steiger, R., et al. 1995, Sci., 268, 1033
Gizon, L., & Duvall, T. L., Jr. 2003, in ESA Special Publication 517, GONG+ 2002 Local and Global Helioseismology: The Present and Future, ed. H. Sawaya-Lacoste (Noordwijk: ESA), 43
Gosling, J. T. 1990, in AGU Mono. Ser. 58, Physics of Magnetic Flux Ropes, ed. C. T. Russell, E. R. Priest, & L. C. Lee (Washington: AGU), 343
Gosling, J. T. 1997, in AIP Conf. Ser. 385, Robotic Exploration Close to the Sun: Scientific Basis, ed. S. R. Habbal (Washington: AIP), 17
Hundhausen, A. J. 1972, Coronal Expansion and Solar Wind (New York: Springer), 101
Kepko, L., Viall, N. M., Antiochos, S. K., et al. 2016, GeoRL, 43, 4089
Komm, R., Howe, R., Hill, F., et al. 2007, ApJ, 667, 571

Laming, J. M. 2015, LRSP, 12, 1
Laming, J. M., Feldman, U., Schühle, U., et al. 1997, ApJ, 485, 911
Landi, E. 2008, ApJ, 685, 1270
Lin, R. P., & Kahler, S. W. 1992, JGRA, 97, 8203
Linker, J. A., Lionello, R., Mikić, Z., Titov, V. S., & Antiochos, S. K. 2011, ApJ, 731, 110
Long, D. M., Williams, D. R., Régnier, S., & Harra, L. K. 2013, SoPh, 288, 567
Lynch, B. J., Edmondson, J. K., Kazachenko, M. D., & Guidoni, S. E. 2016, ApJ, 826, 43
Manoharan, P. K. 2012, ApJ, 751, 128
McComas, D. J., Ebert, R. W., Elliott, H. A., et al. 2008, GeoRL, 35, L18103
Meyer, J.-P. 1985, ApJS, 57, 151
Pariat, E., Dalmasse, K., DeVore, C. R., Antiochos, S. K., & Karpen, J. T. 2015, A&A, 573, A130
Parker, E. N. 1958, ApJ, 128, 664
Parker, E. N. 1979, Cosmical Magnetic Fields: Their Origin and Their Activity (New York: Oxford Univ. Press)
Priest, E., & Forbes, T. 2000, Magnetic Reconnection (Cambridge: Cambridge Univ. Press), 612
Rappazzo, A. F., Velli, M., Einaudi, G., & Dahlburg, R. B. 2005, ApJ, 633, 474
Raymond, J. C., Kohl, J. L., Noci, G., et al. 1997, SoPh, 175, 645
Schatten, K., Wilcox, J. W., & Ness, N. F. 1969, SoPh, 9, 442
Schrijver, C. J., Title, A. M., van Ballegooijen, A. A., Hagenaar, H. J., & Shine, R. A. 1997, ApJ, 487, 424
Schrijver, C. J., Title, A. M., Yeates, A. R., & DeRosa, M. L. 2013, ApJ, 773, 93
Seligman, D., Petrie, G. J. D., & Komm, R. 2014, ApJ, 795, 113
Sheeley, N. R., Wang, Y.-M., Hawley, S. H., et al. 1997, ApJ, 484, 472
Sheeley, N. R., Jr., Lee, D. D.-H., Casto, K. P., Wang, Y.-M., & Rich, N. B. 2009, ApJ, 694, 1471
Simon, G. W., & Leighton, R. B. 1964, ApJ, 140, 1120
Suess, S. T., Wang, A.-H., & Wu, S. T. 1996, JGRA, 101, 19957
Taylor, J. B. 1974, PhRvL, 33, 1139
Taylor, J. B. 1986, RvMP, 58, 741
Timothy, A. F., Krieger, A. S., & Vaiana, G. S. 1975, SoPh, 42, 135
Titov, V. S., Mikić, Z., Linker, J. A., Lionello, R., & Antiochos, S. K. 2011, ApJ, 731, 111
Tokumaru, M., Kojima, M., & Fujiki, K. 2010, JGRA, 115, A04102
Viall, N. M., & Vourlidas, A. 2015, ApJ, 807, 176
von Steiger, R., Geiss, J., & Gloeckler, G. 1997, in Cosmic Winds and the Heliosphere, ed. J. R. Jokipii, C. P. Sonett, & M. S. Giampapa (Tucson: Univ. Arizona Press), 581
von Steiger, R., Schwadron, N. A., Fisk, L. A., et al. 2000, JGR, 105, 27217
von Steiger, R., & Zurbuchen, T. H. 2016, ApJ, 816, 13
von Steiger, R., Zurbuchen, T. H., Geiss, J., et al. 2001, SSRv, 97, 123
Wang, Y.-M., Hawley, S. H., & Sheeley, N. R., Jr. 1996, Sci., 271, 464
Wang, Y.-M., Sheeley, N. R., Socker, D. G., Howard, R. A., & Rich, N. B. 2000, JGRA, 105, 25133
Wang, Y.-M., Sheeley, N. R., Jr., & Rich, N. B. 2007, ApJ, 658, 1340
Warren, H. P., & Brooks, D. H. 2009, ApJ, 700, 762
Zhao, L., Zurbuchen, T. H., & Fisk, L. A. 2009, GeoRL, 36, l14104
Zirker, J. B. 1977, RvGSP, 15, 257
Zurbuchen, T. H. 2007, ARA&A, 45, 297
Zurbuchen, T. H., Fisk, L. A., Gloeckler, G., & von Steiger, R. 2002, GeoRL, 29, 1352
Zurbuchen, T. H., Hefti, S., Fisk, L. A., Gloeckler, G., & von Steiger, R. 1999, SSRv, 87, 353